Volume 19 | Number 9 | 7 May 2019 | Pages 1515–1696

Lab on a Chip

Devices and applications at the micro- and nanoscale

rsc.li/loc

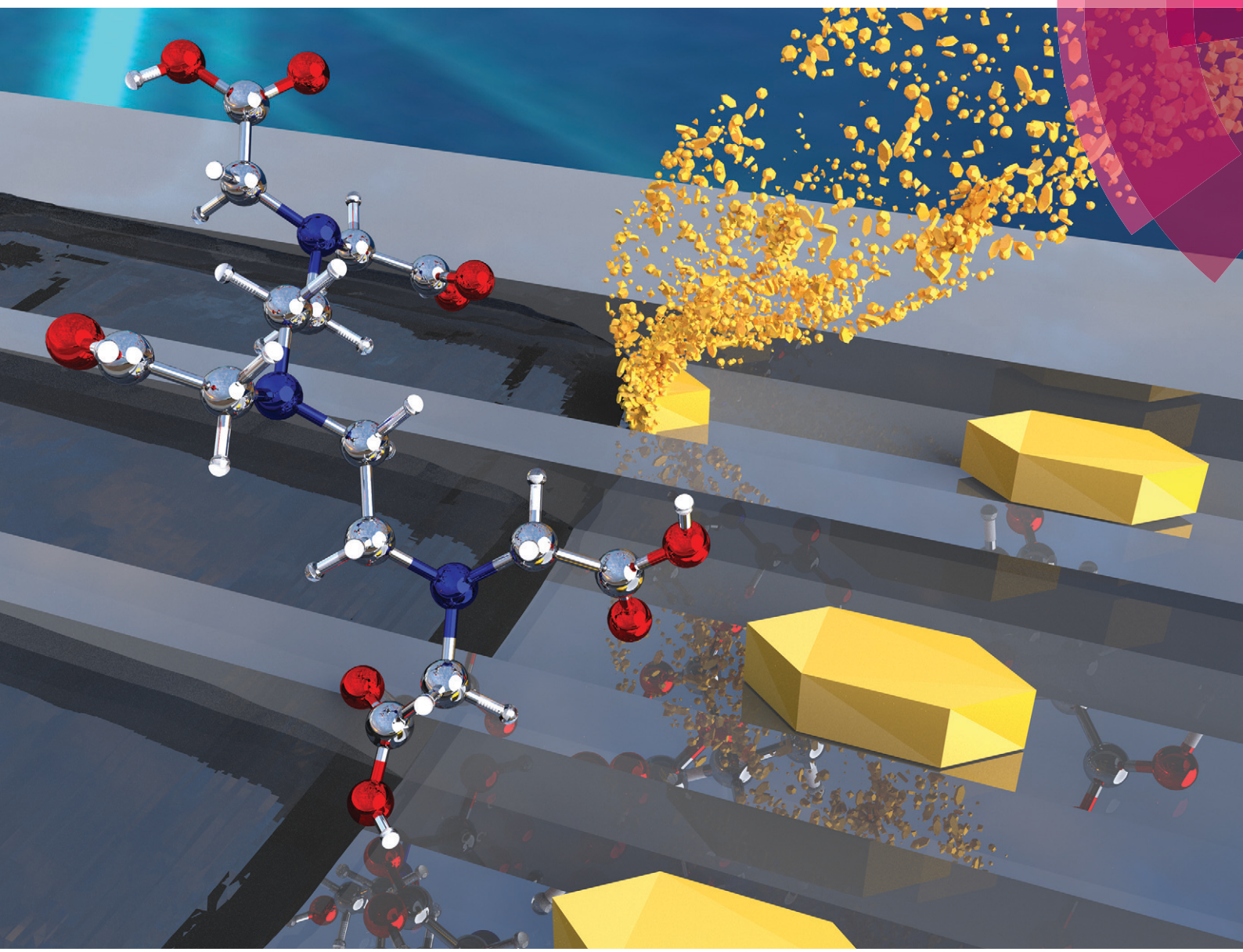

ISSN 1473-0197

ROYAL SOCIETY OF CHEMISTRY | Celebrating IYPT 2019

PAPER

Jeffrey D. Rimer, Jacinta C. Conrad *et al.*

A microfluidic approach for probing hydrodynamic effects in barite scale formation

Lab on a Chip

PAPER

View Article Online
View Journal | View Issue

Cite this: *Lab Chip*, 2019, **19**, 1534

A microfluidic approach for probing hydrodynamic effects in barite scale formation†

Ricardo D. Sosa, ‡[a] Xi Geng,‡[a] Michael A. Reynolds, [b] Jeffrey D. Rimer *[a] and Jacinta C. Conrad *[a]

Received 19th January 2019,
Accepted 26th March 2019

DOI: 10.1039/c9lc00061e

rsc.li/loc

Crystallization of mineral scale components ubiquitously plagues industrial systems for water treatment, energy production, and manufacturing. Chemical scale inhibitors and/or dissolvers are often employed to control scale formation, but their efficacy in flow conditions remains incompletely understood. We present a microfluidic platform to elucidate the time-resolved processes controlling crystallization and dissolution of barite, a highly insoluble and chemically resistant component of inorganic scale, in the presence of flow. In a growth environment, increasing the flow rate leads to a crossover from a transport-limited to a reaction-limited kinetic regime. *In situ* optical microscopy reveals that addition of diethylenetriaminepentaacetic acid (DTPA), a common dissolution agent, alters the morphology of barite crystals grown under flow. In a dissolution environment (*i.e.* alkaline solutions without barium sulfate), increasing the flux of DTPA, whether by increasing the flow rate or DTPA concentration, enhances the rate of dissolution of barite. Trends in the rate of barite dissolution with DTPA concentration and flow rate indicate an optimal combination of these parameters. The combined use of microfluidics and optical microscopy provides a robust and broadly-useful platform for capturing crystallization kinetics and morphological transformation under dynamic flow conditions.

Introduction

Mineralization of highly insoluble compounds during oil and gas production, water treatment, and manufacturing processes may severely damage equipment and result in reduction or loss of finished products, thus posing a serious challenge for these industries.[1,2] The generation of supersaturated fluid, accentuated by changes in temperature, pressure, and flow, can result in the precipitation of multiple inorganic scale components.[2,3] Furthermore, the North American shale boom has highlighted the need for new techniques for studying inorganic scale in the pores of tight shales, where porosity is high (8–10%) while pore size (1–100 nm) and permeability (<0.1 mD) are low.[4] Barite is a commonly encountered and water insoluble scale component (K_{sp} = 1.08 × 10^{-10} at 25 °C) in the oil and gas industry and difficult to treat.[1,5] A lack of available chemical treatments has led the industry to use mechanical means for barite scale remediation, including drill-based milling.[6] Controlling its formation requires a fundamental understanding of growth, inhibition, and dissolution mechanisms in dynamic environments. Barite mineralization occurs *via* classical growth pathways with second-order kinetics.[7–9] Co-precipitation of Ba^{2+} with Sr^{2+}, Ra^{2+}, and other metal ions adds to the complexity of barite formation. Suppressing crystal growth requires the use of molecular additives that, through various modes of action, retard barite precipitation. Surprisingly few compounds have been successfully used in treatments to dissolve barite. Chelating agents represent one class of compounds used to dissolve scale: ethylenediaminetetraacetic acid (EDTA), diethylenetriaminepentaacetic acid (DTPA), and similar polyprotic acids have been commercially employed as scale inhibitors and dissolving agents,[1,10–13] and certain 18-membered macrocycles have been shown to be effective chelators of Ba^{2+} ions.[14] Collectively, studies investigating the effect of additives largely focus on prevention and dissolution mechanisms in quiescent conditions. Scale, however, typically forms under dynamic flow conditions. Understanding the effects of fluid flow on barite crystallization processes is thus expected to improve the design of scale treatments.

A majority of barite mineralization studies under quiescent conditions have investigated crystallization kinetics using bulk assays or in batch processes by tracking solute depletion (conductivity, turbidity, or elemental analysis) or characterizing temporal changes in crystal size and morphology *via ex situ* microscopy (optical, scanning electron, or scanning

[a] *Department of Chemical and Biomolecular Engineering, University of Houston, Houston, TX 77204-4004, USA. E-mail: jrimer@central.uh.edu, jcconrad@uh.edu*
[b] *Shell Exploration and Production Company, Houston, TX 77079, USA*
† Electronic supplementary information (ESI) available. See DOI: 10.1039/c9lc00061e
‡ These authors contributed equally to this work.

probe).[9,15–19] These techniques capture crystallization kinetics that may be influenced by mass transport limitations or require rigorous and time-consuming experimental methods. Kinetic studies relying on the measurement of target ion concentration (conductivity or ion selective analysis) may be vulnerable to interference from spectator ions. Growth, inhibition, and dissolution mechanisms have also been probed in various chemical environments through the use of *in situ* atomic force microscopy (AFM), which provides insight on surface phenomena such as etch pit kinetics, hydration structure, and modes of action of modifiers.[20–28] For growth, interfacial studies have been shown to correlate well with bulk (macroscopic) kinetics.[29] Although the combination of bulk crystallization and crystal surface kinetics provides valuable insight into crystallization mechanisms, microscopic studies (AFM) are limited by a specified set of parameters per trial, sample size, and flow rate range. Furthermore, in AFM studies the flow patterns may be influenced by fluid cell design, and crystallization kinetics can be affected by tip interference with solute transport.[30,31] There remains a need for nonpervasive *in situ* methods that probe crystallization processes under flow while allowing for efficient parametric analyses. Microfluidics offers an excellent alternative for addressing the limitations of traditional methods by eliminating external interference and enabling the sampling of multiple parameters simultaneously under stable flow conditions.

Droplet microfluidics, as one example, allows single crystal nucleation and growth to be decoupled in high-throughput platforms.[32–37] Temporal changes in solution conditions within the droplets (*e.g.* supersaturation), however, preclude facile measurement of anisotropic crystal growth rates. As a second example, single-phase microfluidic platforms used to investigate organic and inorganic crystallization bridge the gap between bulk crystallization measurements and interfacial studies.[38–42] These studies have demonstrated that flow of adjoining solute streams imposes mass transport limitations, which affect local stability of supersaturation within microchannels and thus govern crystallization kinetics as well as nucleation and growth mechanisms of minerals such as calcium carbonate ($CaCO_3$). These mass transport limitations have been shown to influence $CaCO_3$ growth in the presence of inhibitors.[42–44] Microfluidics as a tool for mineralization studies has been applied to other forms of scale, such as gypsum ($CaSO_4{\cdot}2H_2O$) and $CaCO_3$, and integrated with methods such as synchrotron Fourier transform infrared spectroscopy to show that the absence of convection extends the lifetime of typically unstable polymorphs of $CaCO_3$ in confinement.[41] The emerging use of microfluidics for crystallization studies demonstrates the promise for time-resolved measurements of individual crystals. Hence microfluidic techniques represent an ideal platform to explore the effect of flow velocity on crystallization processes for sparingly soluble minerals such as barite.

In this work we develop a microfluidic platform for rapid screening of barite growth, inhibition, and dissolution kinetics under controlled hydrodynamic conditions. Under a pseudo-steady-state growth environment, increasing the solution flow rate of $Ba^{2+}_{(aq)}$ drives a transition in the crystallization kinetics from a transport-limited to a reaction-controlled regime, parameterized by a local Péclet number that describes transport through the boundary layer adjacent to the crystal surface. Coupling the microfluidic platform with optical microscopy enables time-resolved observation of anisotropic crystal growth, revealing face-specific inhibition in the presence of commercial chemical additives. Finally, we demonstrate the versatility of the microfluidic platform by showing that barite dissolution is promoted under flow of alkaline aqueous solutions. These methods provide new insights into the effects of dynamic conditions on mineralization processes. Moreover, our approach allows bulk dissolution phenomenon to be systematically elucidated in a controlled laminar flow environment using a combination of optical microscopy and microfluidics.

Experimental methods

Materials

The following reagents were purchased from Sigma Aldrich: barium chloride dihydrate (99+%), sodium sulfate (>99%), diethylenetriaminepentaacetic acid (DTPA) (>99%), sodium hydroxide (>97%), and sodium chloride (>99.5%). Polydimethylsiloxane (PDMS, Dow Corning SYLGARD 184) was purchased from Essex Brownell. SU-8 2150 photoresist and SU-8 developer were purchased from Microchem. All chemicals were used as received without further purification. Silicone tubing was purchased from Cole-Parmer. Single side polished 4 in P-type silicon wafers <100> were purchased from University Wafer and were cleaned using a piranha solution. Deionized (DI) water (18.2 MΩ·cm) filtered with an Aqua Solutions RODI-C-12A purification system was used in all experiments.

Fabrication of microfluidic devices

The microfluidic platform consisted of two chips placed in series: a chip with a concentration gradient generator was linked downstream with a chip featuring individual straight channels (Fig. 1). The microchannel design, which was adapted from gradient generators in the literature,[45–47] was drafted using AutoCAD software (Autodesk) and fabricated using standard photolithography and polymer casting techniques.[48] A negative photoresist with 400 μm thick features was patterned on a 4-inch silicon wafer using photolithography. Subsequently, a mixture of PDMS prepolymer and curing agent (volume ratio of 10 : 1) was degassed for 30 min and poured over the microchannel molds to 7 mm thickness. PDMS molds were cured at 65 °C for 4 h, after which devices were extracted with a razor blade. Inlet and outlet ports were created using a 2 mm biopsy punch. PDMS devices were cleaned with scotch tape to remove any dust and organic debris. Glass substrates were carefully washed with DI water and isopropyl alcohol and dried with N_2 gas. PDMS devices

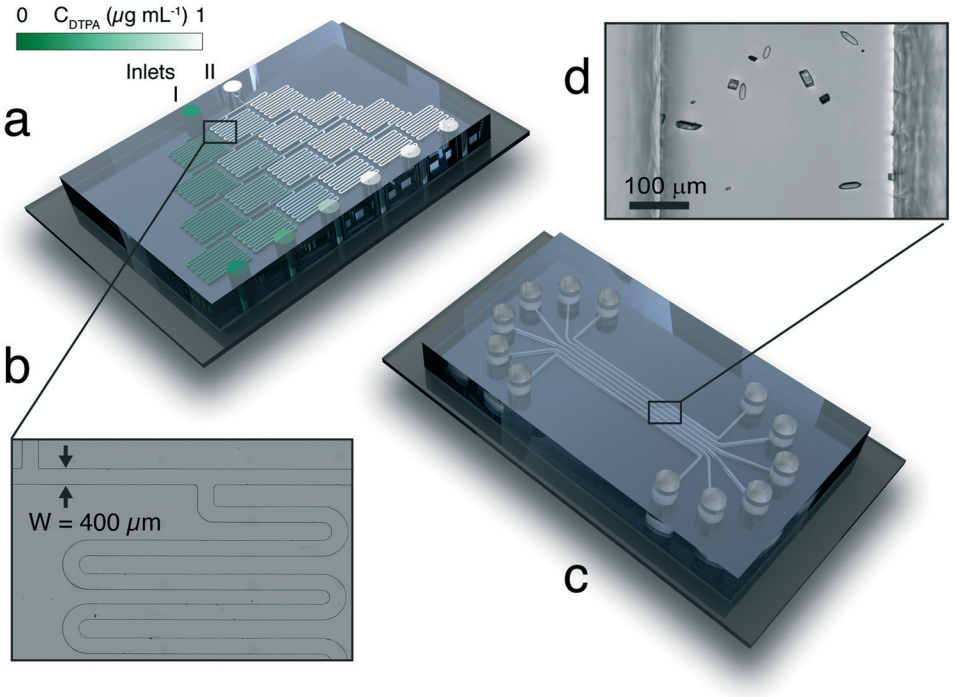

Fig. 1 Microfluidic platform used for inhibition and dissolution studies. (a) Three-dimensional rendering of the gradient generator. The color bar represents the concentration of DTPA in solution: green indicates a concentration of 0 μg mL^{-1} DTPA, and white indicates a concentration of 1 μg mL^{-1} for inhibition studies or 500 μg mL^{-1} for dissolution. The cross-sectional area of all channels is 400 × 400 μm^2. For inhibition studies, growth solution is flowed into inlet I and growth solution with the desired amount of DTPA inhibitor at supersaturation ratio S = 7 is flowed into inlet II. The COMSOL simulation was performed at a flow rate of 12 mL h^{-1}. (b) Optical micrograph of the microchannels in the gradient generator, indicating the width of the microchannel is 400 μm. (c) The gradient generator feeds into a microfluidic device for seeded growth and visualization of barite crystals. The device consists of six microchannels of cross-sectional area 400 × 400 μm^2 and length 5 cm. (d) Representative optical micrograph of the straight microchannels in the second device containing barite seed crystals of 35 μm average length.

were bound onto the glass substrates after corona plasma treatment using a BD-10A high-frequency generator.

Bulk crystallization assays

Barite crystals were synthesized using a protocol modified from procedures reported in the literature.[9,10,29,49–51] In a typical synthesis, $NaCl_{(aq)}$ was first added into a 20 mL glass vial followed by aliquot addition of 10 mM $BaCl_{2,(aq)}$ and 10 mM $Na_2SO_{4,(aq)}$ stock solutions under mild agitation for 10 s. Samples containing molecular modifier DTPA were prepared by adding aliquots of $DTPA_{(aq)}$ to the reaction mixture prior to the addition of Na_2SO_4. The final growth solutions with a total volume of 10 mL had a pH of 7.1 ± 0.3 and a composition of 0.5 mM $BaCl_2$: 0.5 mM Na_2SO_4: 600 mM NaCl: x μg mL^{-1} modifier ($0 \leq x \leq 10$). The pH of growth solutions was measured using an Orion 3-Star Plus pH benchtop meter equipped with a ROSS Ultra electrode (8102BNUWP). The sample vials were left undisturbed at 22 °C for 24 h to allow crystallization of hexagonal barite platelets with well-defined (001), (210), and (100) facets (Fig. 2a and b).

In situ preparation of seed crystals in the microfluidic channels

For *in situ* crystallization studies, the microchannels (Fig. 1) were first flushed thoroughly with DI water. Growth solutions were then delivered into the channels using a dual syringe pump (CHEMYX Fusion 200) at a rate of 12 mL h^{-1} for 90 min. A solution containing 1.0 mM Ba^{2+} was mixed through a y-connector with a second solution component containing 1.0 mM SO_4^{2-} and 550 mM NaCl to circumvent interfacial crystallization in the microchannel caused by diffusion limitations.

Real-time study of growth, inhibition and dissolution kinetics

Time-resolved imaging of barite crystal growth, inhibition, and dissolution using an inverted optical microscope was performed to quantify the kinetics of barite crystallization. For growth, two solution components were prepared in individual syringes. One solution contained 0.7 mM $BaCl_{2,(aq)}$ and the second solution contained 0.7 mM Na_2SO_4 and 1.2 M NaCl. The two solutions were mixed using an inline flow configuration that produced a final composition of 0.35 mM $BaCl_2$, 0.35 mM Na_2SO_4, and 600 mM NaCl. The fully mixed growth solution was introduced into seeded PDMS chips using a dual syringe pump.

Inhibition studies required the use of two dual syringe pumps, each containing syringes of the same growth solution composition but different quantities of growth modifier (DTPA). The first syringe pump contained syringes prepared with no growth modifier (control) and the second syringe

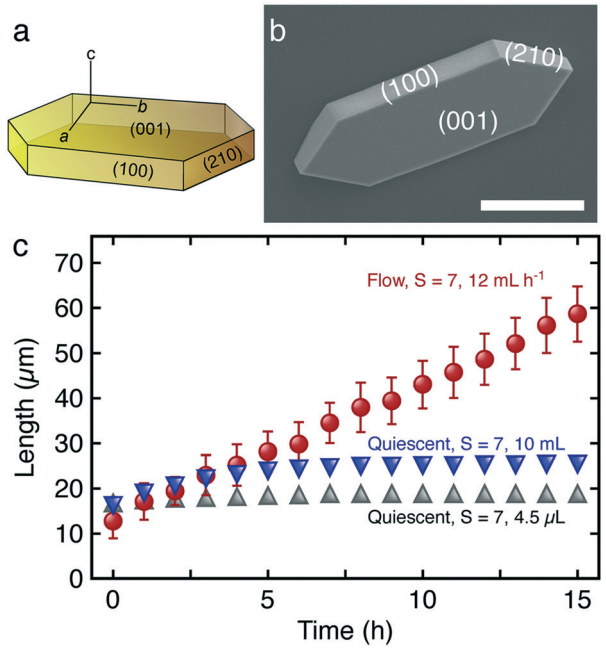

Fig. 2 (a) Barite schematic with crystallographic indices labeled. (b) Barite crystal synthesized at room temperature (22 ± 0.5 °C with 0.5 mM $BaCl_2$: 0.5 mM Na_2SO_4: 600 mM NaCl). Scale bar is equal to 15 μm. (c) Temporal change in barite crystal [010] length during bulk crystallization at room temperature under quiescent conditions (blue triangles represent tests performed in 20 mL vials; grey triangles indicate tests conducted in 4.5 μL microchannels) and under flow of supersaturated growth solution (red circles) in microchannels. Length measurements (symbols) represent an average of at least three individual experiments (for at least 30 crystals per experiment) and error bars indicate two standard deviations across experiments. The error bars for the quiescent experiments are smaller than the symbol size.

pump contained syringes prepared with 1 μg mL^{-1} DTPA, where DTPA was added to the syringe containing SO_4^{2-} to minimize formation of ion complexes. Growth solution components from each dual syringe pump were mixed *via* silicon tubing and a y-connector and successively fed into the corresponding inlet of the concentration gradient generator. Both pumps were programmed with the same flow parameters to ensure a linear concentration gradient at the outlet of the microfluidic channels (Fig. S1 in the ESI†).

Dissolution studies of barite were performed in an alkaline solution that was prepared by adding appropriate amounts of NaOH to DI water. The flow configuration for carrying out barite dissolution entailed a dual syringe pump that fed two separate solutions, one control and one containing 500 μg mL^{-1} $DTPA_{(aq)}$ solution, into the respective inlets of the concentration gradient generator (Fig. 1a). All dissolution cocktails were adjusted to pH 9, which is near the upper limit of the environmentally acceptable pH range for industrial scale treatment.

Microscopic characterization

Barite crystal size and morphology were determined using a Leica DMi8 inverted optical microscope equipped with HC PL Fluotar 5×, 10×, 20×, and N Plan L 50× objectives. At least ten brightfield images of representative areas on the bottom of the glass vials were captured in transmittance mode for characterization of crystals grown in the bulk assay. The average [010] length, [100] width, and [001] thickness of crystals in optical micrographs were measured from a minimum of 90 crystals per trial and three individual trials. An inverted optical microscope equipped with a motorized stage was used to image crystals in the bulk crystallization assays as well as time-resolved crystal growth, inhibition, and dissolution in the microfluidic assays (Fig. S2–S4†). For *in situ* time-resolved studies, LAS X software was used to program a minimum of 10 positions along a seeded microchannel, at which images were captured in transmittance mode at 5 min intervals for at least 3 h. Crystals observed *in situ* were analyzed using ImageJ (NIH) (Fig. S5†). Images were converted to 8 bit followed by a threshold adjustment to outline the edges of barite crystals. An ellipse was fit to each crystal to obtain major and minor axis dimensions corresponding to the length and width of the crystal. At least 90 crystals located in different channels per batch were analyzed over time. Crystal lengths were measured every 5 min during inhibition studies. From the change in crystal length over time, a growth rate r was determined for each experimental condition. The relative growth rate (RGR) was calculated as

$$\mathrm{RGR} = \frac{r_{\mathrm{DTPA}}}{r_{\mathrm{control}}} \quad (1)$$

where r_{DTPA} and r_{control} represent growth rates in the presence and absence of DTPA, respectively.

For *ex situ* microscopy measurements, a clean glass slide (1 × 1 cm^2) was positioned at the bottom of the vials to collect barite crystals. After crystallization, the glass slide was removed from its solution, gently rinsed with DI water, and dried in air prior to analysis. Crystal size and morphology were investigated using a FEI 235 dual-beam focused ion beam scanning electron microscope (SEM). SEM samples were prepared by attaching carbon tape to SEM studs and subsequently attaching glass slides to carbon tape by gently pressing the glass slide to the tape using tweezers. SEM samples were coated with 15–20 nm gold to reduce electron beam charging.

Results and discussion

Barite synthesis in quiescent conditions

Barite crystals grown in a bulk batch synthesis formed hexagonal platelets with an average length of 15 μm and a length-to-width ([010]/[100]) aspect ratio of 2.2 ± 0.2 (Fig. 2a and b). Barite crystals grown under quiescent conditions in the microfluidic channels also formed hexagonal platelets with a length-to-width aspect ratio of 2.4 ± 0.1 (Fig. S6†), nearly identical to that for crystals grown in the batch process at larger volume. Supersaturation and total reservoir volume govern the solute concentration gradient between the bulk

solution and crystal surface. The former provides the driving force for crystal growth, whereas the latter dictates the total time of crystallization.[9,51] Under quiescent conditions, solute transport is dominated by diffusion to the crystal surface through a boundary layer, which can be treated as a stagnant film. As solute is depleted from the bulk, the chemical potential gradient is reduced due to desupersaturation with a concomitant minimization of the driving force for crystal growth. In bulk assays, both nucleation and crystal growth consume solute. The effects of growth on solute consumption can be isolated using the method of seeding, in which seed crystals are grown at supersaturation ratios S in the region of metastability where nucleation does not occur. Under these conditions, S dictates the net change in crystal size.

Design of the microfluidics device

To provide reproducible kinetic data for crystal growth, inhibition, and dissolution with time-resolved imaging, we designed a microfluidic platform to efficiently mix two streams with different concentrations of DTPA (at either supersaturated or undersaturated conditions) and produce a concentration gradient across the six outlet channels (Fig. 1). To ensure complete mixing of two streams, the total length of each serpentine channel was set by the time required for small molecules, such as DTPA (with a diffusion coefficient approximated as $D = 1 \times 10^{-9}$ m^2 s^{-1}),[52] to diffuse across a channel of width $W = 400$ μm to obtain a linear concentration gradient of DTPA at the outlet channels. Specifically, we used the relation $W = \sqrt{tD}$, where $t = AL/Q$ is the minimum residence time of fluid in the microchannels based on the channel length $L = 2.4 \times 10^{-1}$ m, cross-sectional area $A = 1.6 \times 10^{-7}$ m^2, and the maximum volumetric flow rate $Q = 3.3 \times 10^{-8}$ m^3 s^{-1} used in this study. A linear concentration gradient of Ba^{2+} was obtained across the outlets (Fig. S1†), confirming the reliability of the microfluidic concentration gradient generator. This experimental design enables simultaneous testing of multiple concentrations of molecular modifiers for barite dissolution, thus greatly reducing both screening time and the number of individual experiments required. Here we characterized the growth of seed crystals within the channels of the microfluidic device. Performing bulk crystallization studies in a microfluidic device allows individual crystals to be tracked over time and across a broad range of conditions. Thus, microfluidic devices can be used as a platform for rapid parametric analyses of anisotropic crystal growth at a macroscopic scale.

Crystal growth in quiescent and flow conditions

During seeded bulk crystallization experiments in supersaturated solution ($S = 7$) under quiescent conditions, the rate of crystal growth decreases over time, leading to the emergence of a plateau in crystal size as solute is incorporated into the crystals (blue triangles in Fig. 2c). Identical experiments at higher solute concentration ($S = 10$, Fig. S7†) extend the duration of crystal growth beyond what is achieved in less supersaturated media, resulting in larger crystals.

Seeded growth in the small microchannel volume (*ca.* 4.5 μL) under quiescent conditions reveals a twofold reduction in the growth kinetics of barite compared to measurements in a batch process using larger volume (20 mL) vials. Barite crystals grown at $S = 7$ in the microfluidic channels (grey triangles in Fig. 2c) increase only slightly in size over time, commensurate with the rapid depletion of solute from the growth solution in a smaller volume. This observation confirms that the relatively small volume of each individual microchannel leads to a more rapid reduction of the driving force for crystal growth. Furthermore, we observe that the growth rate of crystals is uniform across microchannels (Fig. S8†). Because concentration gradients in solute would generate corresponding gradients in crystal number density and size,[42–44,53–55] which are not observed in these measurements, this result confirms that aqueous solutes are fully mixed in our device.

In addition to enabling *in situ* imaging during growth, a key advantage of microfluidic devices for studies of crystallization is the ability to generate well-defined flow conditions. Seeded crystal growth experiments confirm that faceted barite crystals can be obtained uniformly across microchannels owing to the complete mixing of inlet solutions (Fig. S8†), which allows macroscopic growth kinetics to be quantified under laminar flow (for Reynolds numbers Re of $0.92 < \mathrm{Re} < 92$). To identify the transport process that controls the delivery of solute, we calculate a macroscopic Péclet number $\mathrm{Pe}_{\mathrm{macro}} = Wv/D$, where v is the average fluid velocity across the microchannel, $W = 400$ μm is the channel width, and $D = 8.47 \times 10^{-10}$ m^2 s^{-1} is the diffusivity of Ba^{2+} ions in water. In our experiments $\mathrm{Pe}_{\mathrm{macro}}$ varies from 10^3 to 10^5 and advection governs transport of solute across microchannels,[55] in accord with the uniformity in crystal size observed across the width of the channel. Under flow of supersaturated solution, the driving force for crystallization is constant because solute is continuously replenished; therefore, seeded growth in the microfluidic device under continuous flow and the same solute concentration ($S = 7$, red circles in Fig. 2c) results in crystals of sizes much larger than those produced *via* quiescent batch synthesis ($S = 7$, blue triangles in Fig. 2c). The length of crystals grown under flow increases linearly with time, indicating that the constant supersaturation produces a steady driving force for crystal growth.

The fluid flow rate affects crystal growth kinetics during continuous crystallization processes. Microfluidics enables the rate of solute delivery to be tuned *via* the flow rate in the laminar regime. In this regime, the boundary layer thickness δ on a crystal of length x in a square channel of width W is proportional to $\mathrm{Re}^{-1/2}$,[56–58]

$$\delta = 5\left(\frac{D}{v}\right)^{\frac{1}{3}}\left(\frac{Wx}{\mathrm{Re}}\right)^{\frac{1}{2}}. \quad (2)$$

Increasing the flow rate narrows the boundary layer and thereby reduces the time for solute to diffuse to the crystal

surface. Thus, increasing the flow rate of barite growth solution is anticipated to lead to an increase in crystal growth kinetics until the growth rate is limited by the rate at which solute incorporates in the crystal surface. In a reaction-controlled regime, the crystal growth kinetics reflect adsorption/desorption of solute ions/molecules at the crystal surface established by supersaturation.

We investigate the relative importance of transport *versus* surface kinetics by varying the flow rate in the microfluidic device. The rate of crystal growth increases monotonically when the flow rate is lower than 12 mL h^{-1} (Re < 9.2) (Fig. 3). This result indicates that the rate of solute delivery to the crystal surface controls the crystal growth rate. When flow rates are higher than 12 mL h^{-1} (Re > 9.2), the barite growth rate plateaus at 4 μm h^{-1} and does not change even when the flow rate is further increased. The independence of crystal growth rate from flow rate indicates a transition to a reaction-controlled regime on the macroscopic scale.

The macroscopic Péclet number, describing the diffusion of solute across the channel, ranges between $10^3 < Pe_{macro} < 10^5$. Crystallization typically depends on diffusion of solute through the stagnant boundary layer near the crystal surface. We define a local Péclet number $Pe_{local} = \delta v/D$, where the relevant length scale is the boundary layer thickness δ (eqn (2)),[59] that ranges between $140 < Pe_{local} < 1400$. When flow rates are low (Re < 9.2, $140 < Pe_{local} < 435$), crystal growth is controlled by the rate of delivery of solute. Pe_{local} is high in this regime, suggesting that bulk advection still governs solute transport. The dependence of growth kinetics on flow rate suggests that crystal growth is under mixed transport-surface kinetic control. The well-defined flow conditions in the microfluidic device allow us to identify a flow rate regime where mass transport limitations are minimized and crystal growth is predominantly governed by surface kinetics.

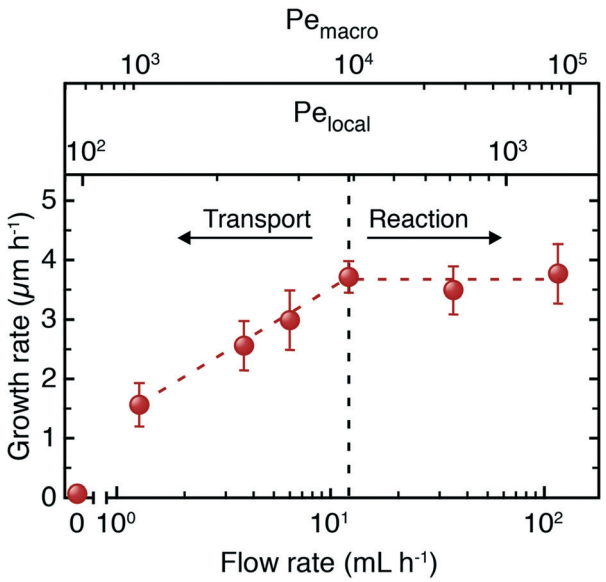

Fig. 3 Effect of flow rate on seeded growth of barite. The growth rate (left axis) was measured by linear regression of length *versus* time data sets over 3 h at room temperature in microchannels (400 μm × 400 μm). The growth solution consisted of 0.35 mM Ba^{2+}: 0.35 mM SO_4^{2-}: 600 mM NaCl with a supersaturation ratio S = 7. Data points represent average growth rates over at least three individual experiments. Dashed lines are fits in each regime (logarithmic in the transport-limited regime and constant in the reaction-limited regime) and error bars equal two standard deviations.

Inhibition of barite growth using a molecular additive

DTPA is a common chelating agent for divalent cations, including barium, and is used commercially to treat scale mineralization.[1,16] Introducing this commercial scale inhibitor in microfluidic growth experiments retards barite growth preferentially along the [010] direction of the crystal, as revealed using time-resolved optical microscopy (Fig. 4a). The apical tips become blunted over time, suggesting that growth is inhibited along the crystal length, *b*-axis, due to the development of a new facet (Fig. 4a, 3 h image). Analysis of optical micrographs (Fig. S9†) indicates that the new facet corresponds to the (011) plane. This result, coupled with a decrease in aspect ratio (Fig. S9†), suggests that DTPA preferentially binds to the (011) facet of barite. To understand the effects of DTPA on barite growth, we compare to earlier studies using another chelating agent, ethylenediaminetetraacetic acid (EDTA), which shares a similar

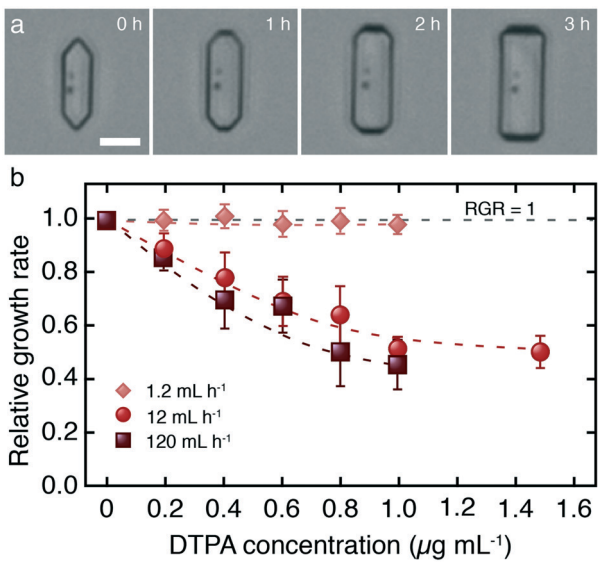

Fig. 4 (a) Time-elapsed optical micrographs demonstrating the effects of 1 μg mL^{-1} DTPA on barite growth under solution flow. The scale bar for all images is equal to 10 μm. The flow rate through the microchannel is 12 mL h^{-1}, corresponding to Re = 9.2 and Pe_{local} = 435. (b) Relative growth rate (RGR) as a function of DTPA concentration for various flow rates. RGR values below unity signify growth inhibition. Each data point represents the average of at least three individual experiments using the microfluidic platform. Error bars indicate two standard deviations. The growth solutions used at both inlets consisted of 0.35 mM Ba^{2+}, 0.35 mM SO_4^{2-}, 600 mM NaCl with S = 7. Solutions for inlet I and inlet II contained 0 μg mL^{-1} and 1 μg mL^{-1} DTPA, respectively. Individual experiments at 1.5 μg mL^{-1} DTPA were conducted to confirm a plateau in RGR. Dashed lines are interpolations to guide the eye. All experiments were conducted at room temperature and pH 7.

backbone structure with DTPA but contains three fewer CH_2 groups, one fewer amine moiety, and one fewer carboxylic acid group. Carboxylates such as EDTA and DTPA are often assumed to modify crystal growth by forming complexes with divalent cations and lowering the supersaturation. At low modifier concentration, however, we observe that DTPA principally inhibits barite crystallization through adsorption on crystal surfaces, which impedes solute incorporation. Adsorption of EDTA was reported to be energetically more favorable on the (011) facet of barite.[12,19] This comparison between two crystal growth modifiers suggests that both polyprotic acids appear to operate under similar modes of action, despite differences in their physicochemical properties.

Quiescent studies confirm that DTPA is an inhibitor of barite crystallization. Given that fluid flow also affects barite growth kinetics in the laminar regime, we hypothesize that the inhibition mechanism and efficacy of DTPA may be affected by the fluid flow rate. To probe the effects of fluid flow on inhibition of barite in the presence of DTPA, we conducted *in situ* microfluidic experiments at flow regimes where growth in the absence of DTPA is controlled by either mass transport or surface kinetics. At a low flow rate (1.2 mL h^{-1}; Re = 0.92; Pe_{local} = 140) barite growth kinetics are independent of DTPA concentration (Fig. 4b, diamonds), although slight blunting of the apical tips is observed in optical micrographs (Fig. S10†). The lack of dependence of crystal growth on modifier concentration at low flow rate is indicative of mass transport limitations (*i.e.*, the organic modifier exhibits a slower rate of diffusion compared to more mobile Ba^{2+} and SO_4^{2-} ions). The longer diffusion time for DTPA, relative to the mobile ions, suggests that its coverage on crystal surfaces at thermodynamic equilibrium may be difficult to achieve even at high DTPA concentrations; this idea is consistent with the inability of DTPA to inhibit crystal growth at low flow rates. Conversely, time-resolved optical micrographs of barite crystal growth acquired at a higher flow rate of 12 mL h^{-1} reveal that the crystal morphology changes with increasing DTPA concentration to generate new {011} facets (Fig. S9†), suggesting that DTPA preferentially binds to sites located on {210} surfaces.

Relative growth rate (RGR) and crystal morphology of barite depend more strongly on DTPA concentration at higher flow rates. At a flow rate of 12 mL min^{-1} (Re = 9.2; Pe_{local} = 435), the RGR of barite initially decreases monotonically with increasing DTPA concentration and reaches a plateau near 1 μg mL^{-1} DTPA (Fig. 4b, circles) that corresponds to 55% inhibition of crystal growth. The plateau in RGR suggests that inhibitor coverage on crystal surfaces approaches thermodynamic equilibrium, and that barite growth in this fluid flow regime is kinetically controlled by advection of solute to growth sites on the crystal surface (Pe_{local} = 435). The molar ratio of DTPA/Ba^{2+} is less than 0.005, indicating the effect of modifier sequestration of Ba^{2+} ions is negligible compared to those imposed by DTPA-crystal interactions.

Under the highest flow rate condition tested (120 mL h^{-1}; Pe_{local} = 1400; Re = 92), the RGR again decreases with increasing DTPA concentration (Fig. 4b, squares), reaching a maximum *ca.* 60% inhibition of barite growth. An order of magnitude increase in flow rate leads to a negligible increase in DTPA efficacy (as the RGRs at 12 and 120 mL h^{-1} are equivalent within the error of measurement). Collectively, these studies indicate that barite crystallization at flow rates of 12 mL h^{-1} or higher (Re ≥ 9.2) in the laminar regime is controlled by surface kinetics. Inhibitor efficacy is influenced by flow, which suggests that eliminating mass transport limitations is necessary to maximize barite inhibition. Overall, the microfluidic platform allowed us to elucidate preferential binding modes of DTPA on barite in real time and confirm that an increase in flow enhances inhibition of barite growth.

Barite dissolution in the presence of DTPA

Barite dissolution has been widely investigated in the presence and absence of organic ligands. In pure water under flow, the basal surface of barite is mostly stable with a slow rate of formation of shallow etch pits.[20,60] In ligand-promoted dissolution, the Ba-DTPA complex is most stable at pH ≥ 12 where DTPA is fully deprotonated. Due to this stability, $DTPA^{5-}$ anions chelate surface barium and weaken the Ba–SO_4 bonds.[62] DTPA may coordinate with multiple surface barium atoms and promote dissolution in an aqueous environment with desorption of the surface being the rate-limiting step.[18,20,61–65] Dissolution ultimately occurs *via* hydration of surface barium atoms. The effects of flow rate, however, have remained elusive and the magnitude of the flow velocity is likely to affect dissolution kinetics.

We investigated the importance of flow and the role of DTPA for the dissolution of barite in microchannels using alkaline solutions (10 μM NaOH, pH 9) in the absence of barium sulfate. In quiescent conditions, exposure to DTPA for 4 h negligibly affected the morphology and size of barite crystals (Fig. 5a). This result is inconsistent with previous reports of DTPA-promoted dissolution in quiescent conditions with larger reservoir volumes,[16] suggesting that the finite volume (4.5 μL) of solution in the microchannels under quiescent conditions may not contain sufficient amounts of DTPA to promote macroscopic dissolution. Interestingly, barite crystals exposed to flow using the same alkaline solution, but without DTPA, did not exhibit macroscopic changes in size or morphology (Fig. 5b). This result, however, is consistent with previous reports that indicate a low solubility of barite in alkaline solution.[61] By contrast, striking differences in final barite crystal morphology and size are observed when 500 μg mL^{-1} DTPA is flowed through the seeded microchannels. Optical micrographs reveal significant deterioration of the seed crystal over a 4 h experiment (Fig. 5c). Although DTPA is not fully dissociated ($DTPA^{4-}$) at the pH of our experiments, these results are in accord with bulk dissolution experiments in the presence of stirring, which demonstrate deep etch pit

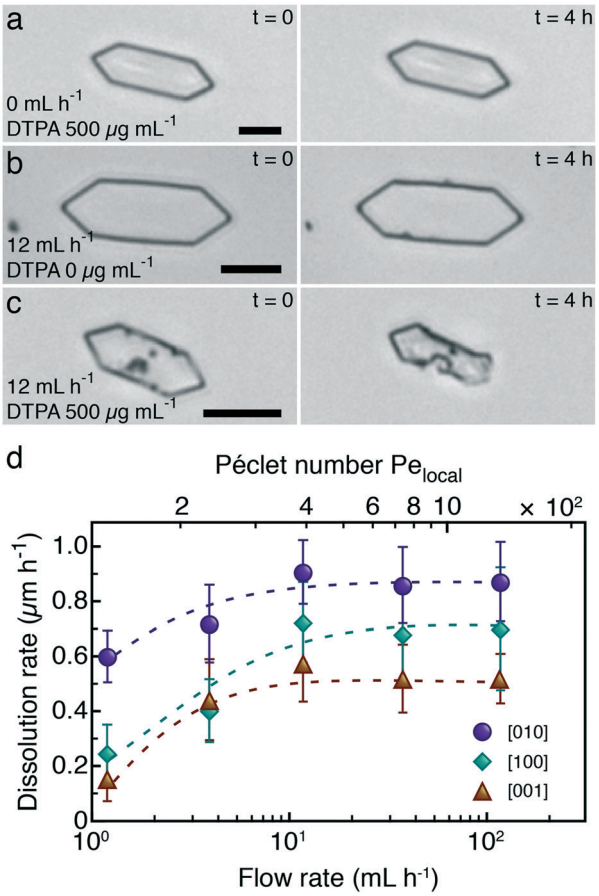

Fig. 5 Imaging and analysis of barite dissolution in alkaline media. Initial and final micrographs of barite seed crystals (a) in the presence of 500 μg mL^{-1} DTPA and quiescent conditions, (b) in the absence of DTPA under flow (12 mL h^{-1}), and (c) in the presence of 500 μg mL^{-1} DTPA under the same flow rate. Solutions used for dissolution did not contain barium sulfate, and were adjusted to pH = 9 with appropriate amounts of NaOH. The scale bar for all images is equal to 10 μm. Dissolution experiments were conducted at room temperature (22 ± 0.5 °C) for a minimum of 4 h. (d) Dissolution rate of barite as a function of flow rate ($0.92 < Re < 92$; $140 < Pe_{local} < 1400$) using crystal length ([010]), width ([100]), and thickness ([001]) measurements over time. Dashed lines are guides to the eye.

formation and crystal dissolution at higher pH where DTPA is fully dissociated and $DTPA^{5-}$-Ba^{2+} chelation is optimal.[17]

We characterized the evolution of barite seed crystal length, width, and thickness under flow of 500 μg mL^{-1} DTPA at various rates ($0 < Re < 92$; $0 < Pe_{local} < 1400$). Dissolution occurs fastest along the [010] direction and appears to be nearly independent of flow rate. By contrast, barite mass loss along the [100] and [001] directions increases with flow rate and plateaus at rates above 3.6 mL h^{-1} ($168 < Pe_{local} < 1400$) indicating surface reaction-controlled kinetics (Fig. 5d). These results differ from dissolution kinetics reported for mineral dolomite using a rotating disk, which did not depend on flow rate within the laminar regime.[66] These differences may be attributed to disparate experimental conditions and/or physicochemical properties of minerals. For barite, fast dissolution along the *b*-axis is consistent with microscopic observations of ligand-promoted dissolution in which etch pits propagate along the [010] direction, suggesting these microfluidic experiments may provide insight on microscopic surface dissolution. In contrast to reported etch pit formation rates where propagation along the *b*-axis is 2.5 times greater than along the *a*-axis, dissolution rates along the [010] direction are comparable to rates in the [100] direction under flow in microchannels.[60]

In separate experiments, we varied the DTPA concentration of undersaturated solutions ($S = 0$) and measured the

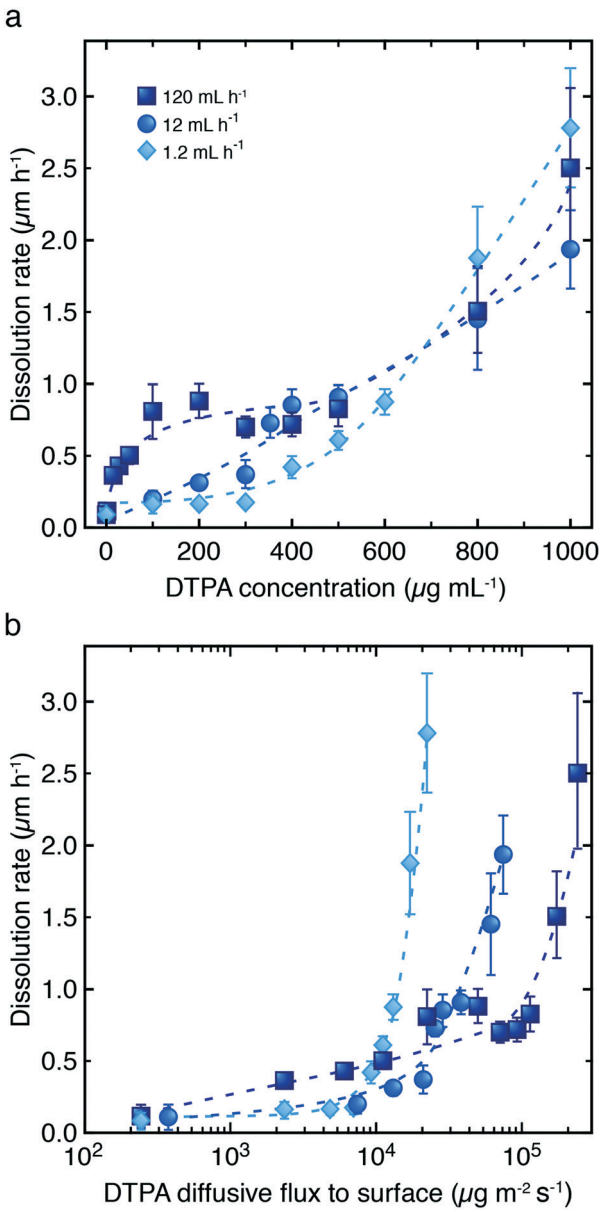

Fig. 6 Rate of dissolution of barite seeds as a function of (a) DTPA concentration and (b) diffusive flux of DTPA to the crystal surface, as measured by changes in crystal length along the [010] direction. All solutions were prepared in the absence of barium sulfate and were adjusted to pH = 9 with appropriate amounts of NaOH. Experiments were conducted at room temperature (22 ± 0.5 °C) for a minimum of 4 h. Error bars represent two standard deviations and dashed curves are guides to the eye.

extent of barite dissolution at several flow rates (Fig. 6). The alkalinity of solutions in these experiments was adjusted to pH = 9, the approximate upper limit for environmentally acceptable standards,[67] such that DTPA is not fully deprotonated (*i.e.* the predominant species is $DTPA^{4-}$). These conditions are in contrast to those of previous DTPA-promoted dissolution experiments that were carried out at higher pH (both quiescent and stirred), allowing for full deprotonation.[16,17,60] Increasing DTPA concentration enhances the dissolution rate for all flow rates evaluated in this study ($0 < Pe_{local} < 1400$). At a low flow rate (1.2 mL h^{-1}), the rate of dissolution increases monotonically with increasing DTPA concentration. At a higher flow rate (12 mL h^{-1}), the dissolution rate increases linearly with concentration. Under much higher flow rate (120 mL h^{-1}), the rate of barite dissolution initially increases sharply with concentration, then increases linearly at higher flow rates. At concentrations below 500 μg mL^{-1} dissolution is enhanced by an increase in flow rate. At higher concentrations, dissolution is linearly dependent on DTPA concentration and becomes independent of flow rate. While the underlying physics governing the trends in dissolution rates at lower DTPA concentrations remains unknown, these results indicate that the dependence of dissolution kinetics on DTPA concentration is influenced by changes in flow rate within a finite concentration regime.

We calculated the boundary layer profiles for barite under each flow rate tested experimentally (Fig. S11–S14†) and the diffusive flux of DTPA to the crystal surface (Fig. S15†), $J = Dc_o/\delta$, to probe the dissolution kinetics of barite. For a fixed flow rate, the diffusive flux is dependent on the change in DTPA concentration from the bulk to the crystal surface. Given that an increase in either flow rate or DTPA concentration enhances dissolution, we hypothesize that dissolution is controlled by the mass flux of DTPA to the surface. In support of this hypothesis, the rate of dissolution for barite is enhanced with increasing diffusive flux under all flow rates. A majority of studies in literature[60,62,63] use DTPA concentrations that are 10- to 100-times greater than those employed in this study, and observe that the dissolution rates of barite first increase and then decrease with concentration. The results of our study suggest that there may be different, albeit unknown, molecular processes governing DTPA-induced dissolution of barite crystals. Additional microscopic studies are needed to fully resolve the physical processes governing the behavior in Fig. 6; nevertheless, barite dissolution is markedly enhanced under specific flow conditions that depend on DTPA concentration.

Conclusion

We present a microfluidic platform for investigating bulk crystallization and dissolution kinetics of barite in dynamic flow conditions. We systematically investigate hydrodynamic contributions by varying the flow rate during crystallization of barite in the presence and absence of the scale inhibitor DTPA, and obtain time-resolved characterizations of crystal morphology for each case. Under flow of supersaturated growth solution, barite growth undergoes a transition from mass-transport-limited to surface-reaction-limited kinetics at a local Péclet number of ~250. Growth studies in the presence of DTPA reveal that this transport limitation also holds for inhibition of barite at low concentrations of DTPA. In a reaction-limited growth environment, DTPA induces the formation of a new facet, which remains stable through the duration of experiments. In undersaturated conditions, barite dissolution is enhanced with increasing diffusive flux of DTPA to the crystal surface. At low DTPA concentrations, however, our results suggest that dissolution may occur *via* distinct, unique molecular processes that remain to be determined. Identifying these processes likely requires the use of methods, such as atomic force microscopy experiments or molecular simulation, that are capable of resolving dissolution at an atomic level. This microfluidic platform can be extended to characterize the kinetics of crystallization in systems in which hydrodynamics may play a significant role. Barite was chosen for these studies on the basis of its commercial relevance to demonstrate how microfluidics coupled with microscopy could serve as a quantitative method for determining crystal growth and inhibition under dynamic flow conditions. As one example, these techniques could be used to assess the transient surface area for materials for which kinetic parameters are difficult to estimate or determine. Together, these techniques offer an opportunity to investigate the crystal growth kinetics for other problematic and geochemically-relevant biominerals under a controlled flow regime environment.

Conflicts of interest

There are no conflicts to declare.

Acknowledgements

We acknowledge financial support from Shell Oil Company and the National Science Foundation Graduate Student Fellowship (Award DGE 1144207). JCC and JDR also wish to acknowledge support from the Welch Foundation (Awards E-1869 and E-1794, respectively).

References

1 M. Crabtree, D. Eslinger, P. Fletcher, M. Miller, A. Johnson and G. King, *Oilfield Rev.*, 1999, 30–45.
2 J. S. Hanor, *Rev. Mineral. Geochem.*, 2000, **40**, 193–275.
3 D. J. Weintritt and J. C. Cowan, *J. Pet. Technol.*, 1967, **19**, 1381–1394.
4 K. S. Lee and T. H. Kim, *Integrative Understanding of Shale Gas Reservoirs*, Springer International Publishing, 2016.
5 C. W. Blount, *Am. Mineral.*, 1977, **62**, 942–957.
6 T. C. Timmreck and G. Shook, *J. Environ. Health*, 1992, **55**, 22–26.
7 G. H. Nancollas and S. T. Liu, *Soc. Pet. Eng. J.*, 1975, **15**, 509–516.

8 W. H. Leung and G. H. Nancollas, *J. Inorg. Nucl. Chem.*, 1978, **40**, 1871–1875.
9 G. L. Gardner and G. H. Nancollas, *J. Phys. Chem.*, 1983, **87**, 4699–4703.
10 S. N. Black, L. A. Bromley, D. Cottier, R. J. Davey, B. Dobbs and J. E. Rout, *J. Chem. Soc., Faraday Trans.*, 1991, **87**, 3409–3414.
11 K. S. Sorbie and N. Laing, How scale inhibitors work: Mechanisms of selected barium sulphate scale inhibitors across a wide temperature range, *SPE Sixth International Symposium on Oilfield Scale*, Aberdeen, Scotland, United Kingdom, 2004, Manuscript # SPE-87470-MS, DOI: 10.2118/87470-MS.
12 F. Jones, P. Jones, M. I. Ogden, W. R. Richmond, A. L. Rohl and M. Saunders, *J. Colloid Interface Sci.*, 2007, **316**, 553–561.
13 E. Mavredaki, A. Neville and K. Sorbie, *Appl. Surf. Sci.*, 2011, **257**, 4264–4271.
14 N. A. Thiele, S. N. MacMillan and J. J. Wilson, *J. Am. Chem. Soc.*, 2018, **140**, 17071–17078.
15 A. C. Todd and M. D. Yuan, *SPE Prod. Eng.*, 1992, **7**, 85–92.
16 K. Dunn, E. Daniel, P. J. Shuler, H. J. Chen, Y. Tang and T. F. Yen, *J. Colloid Interface Sci.*, 1999, **214**, 427–437.
17 K. Dunn and T. F. Yen, *Environ. Sci. Technol.*, 1999, **33**, 2821–2824.
18 K.-S. Wang, R. Resch, K. Dunn, P. Shuler, Y. Tang, B. E. Koel and T. Fu Yen, *Colloids Surf., A*, 1999, **160**, 217–227.
19 F. Jones and A. L. Rohl, *Mol. Simul.*, 2005, **31**, 393–398.
20 D. Bosbach, C. Hall and A. Putnis, *Chem. Geol.*, 1998, **151**, 143–160.
21 S. R. Higgins, G. Jordan, C. M. Eggleston and K. G. Knauss, *Langmuir*, 1998, **14**, 4967–4971.
22 P. Risthaus, D. Bosbach, U. Becker and A. Putnis, *Colloids Surf., A*, 2001, **191**, 201–214.
23 C. M. Pina, C. V. Putnis, U. Becker, S. Biswas, E. C. Carroll, D. Bosbach and A. Putnis, *Surf. Sci.*, 2004, **553**, 61–74.
24 M. Kowacz, C. V. Putnis and A. Putnis, *Geochim. Cosmochim. Acta*, 2007, **71**, 5168–5179.
25 Y. Kuwahara and M. Makio, *Appl. Geochem.*, 2014, **51**, 246–254.
26 J. N. Bracco, Y. Gooijer and S. R. Higgins, *Geochim. Cosmochim. Acta*, 2016, **183**, 1–13.
27 J. N. Bracco, S. S. Lee, J. E. Stubbs, P. J. Eng, F. Heberling, P. Fenter and A. G. Stack, *J. Phys. Chem. C*, 2017, **121**, 12236–12248.
28 J. Weber, J. N. Bracco, J. D. Poplawsky, A. V. Ievlev, K. L. More, M. Lorenz, A. L. Bertagni, S. A. Jindra, V. Starchenko, S. R. Higgins and A. G. Stack, *Cryst. Growth Des.*, 2018, **18**, 5521–5533.
29 J. R. A. Godinho and A. G. Stack, *Cryst. Growth Des.*, 2015, **15**, 2064–2071.
30 M. Peruffo, M. M. Mbogoro, M. Adobes-Vidal and P. R. Unwin, *J. Phys. Chem. C*, 2016, **120**, 12100–12112.
31 M. Adobes-Vidal, A. G. Shtukenberg, M. D. Ward and P. R. Unwin, *Cryst. Growth Des.*, 2017, **17**, 1766–1774.
32 J.-u. Shim, G. Cristobal, D. R. Link, T. Thorsen and S. Fraden, *Cryst. Growth Des.*, 2007, **7**, 2192–2194.
33 M. Ildefonso, E. Revalor, P. Punniam, J. B. Salmon, N. Candoni and S. Veesler, *J. Cryst. Growth*, 2012, **342**, 9–12.
34 M. Heymann, A. Opthalage, J. L. Wierman, S. Akella, D. M. E. Szebenyi, S. M. Gruner and S. Fraden, *IUCrJ*, 2014, **1**, 349–360.
35 S. Zhang, N. Ferté, N. Candoni and S. Veesler, *Org. Process Res. Dev.*, 2015, **19**, 1837–1841.
36 C. J. J. Gerard, G. Ferry, L. M. Vuillard, J. A. Boutin, N. Ferte, R. Grossier, N. Candoni and S. Veesler, *Cryst. Growth Des.*, 2018, **18**, 5130–5137.
37 R. Grossier, V. Tishkova, R. Morin and S. Veesler, *AIP Adv.*, 2018, **8**, 075324.
38 B. R. Schudel, C. J. Choi, B. T. Cunningham and P. J. A. Kenis, *Lab Chip*, 2009, **9**, 1676–1680.
39 X. Gong, Y.-W. Wang, J. Ihli, Y.-Y. Kim, S. Li, R. Walshaw, L. Chen and F. C. Meldrum, *Adv. Mater.*, 2015, **27**, 7395–7400.
40 G. Laffite, C. Leroy, C. Bonhomme, L. Bonhomme-Coury, E. Letavernier, M. Daudon, V. Frochot, J. P. Haymann, S. Rouzière, I. T. Lucas, D. Bazin, F. Babonneau and A. Abou-Hassan, *Lab Chip*, 2016, **16**, 1157–1160.
41 S. Li, J. Ihli, W. J. Marchant, M. Zeng, L. Chen, K. Wehbe, G. Cinque, O. Cespedes, N. Kapur and F. C. Meldrum, *Lab Chip*, 2017, **17**, 1616–1624.
42 L. Li, J. R. Sanchez, F. Kohler, A. Røyne and D. K. Dysthe, *Cryst. Growth Des.*, 2018, **18**, 4528–4535.
43 S. W. Seo, K. Y. Ko, C.-S. Lee and I. H. Kim, *Hwahak Konghak*, 2013, **51**, 151–156.
44 Y. Zeng, J. Cao, Z. Wang, J. Guo and J. Lu, *Cryst. Growth Des.*, 2018, **18**, 1710–1721.
45 N. L. Jeon, S. K. W. Dertinger, D. T. Chiu, I. S. Choi, A. D. Stroock and G. M. Whitesides, *Langmuir*, 2000, **16**, 8311–8316.
46 S. K. W. Dertinger, D. T. Chiu, N. L. Jeon and G. M. Whitesides, *Anal. Chem.*, 2001, **73**, 1240–1246.
47 T. Ishida, T. Shimamoto, N. Ozaki, S. Takaki, T. Kuchimaru, S. Kizaka-Kondoh and T. Omata, *Micromachines*, 2016, **7**, 155.
48 Y. Xia and G. M. Whitesides, *Annu. Rev. Mater. Sci.*, 1998, **28**, 153–184.
49 G. H. Nancollas and N. Purdie, *Trans. Faraday Soc.*, 1963, **59**, 735–740.
50 C. W. Blount, *Am. Mineral.*, 1974, **59**, 1209–1219.
51 S. T. Liu, G. H. Nancollas and E. A. Gasiecki, *J. Cryst. Growth*, 1976, **33**, 11–20.
52 P. Vanysek, *CRC handbook of chemistry and physics*, 2000, vol. 83, pp. 76–78.
53 S. Walter, S. Malmberg, B. Schmidt and M. A. Liauw, *Catal. Today*, 2005, **110**, 15–25.
54 T. Gervais and K. F. Jensen, *Chem. Eng. Sci.*, 2006, **61**, 1102–1121.
55 T. M. Squires, R. J. Messinger and S. R. Manalis, *Nat. Biotechnol.*, 2008, **26**, 417.
56 V. G. Levich, *Physicochemical hydrodynamics*, Prentice-Hall, Englewood Cliffs, N.J., 1962.
57 A. A. Chernov, *J. Cryst. Growth*, 1992, **118**, 333–347.
58 A. E. S. Van Driessche, J. M. García-Ruiz, J. M. Delgado-López and G. Sazaki, *Cryst. Growth Des.*, 2010, **10**, 3909–3916.

59 N. M. Juhasz and W. M. Deen, *Ind. Eng. Chem. Res.*, 1991, **30**, 556–562.
60 A. Putnis, J. L. Junta-Rosso and M. F. Hochella, *Geochim. Cosmochim. Acta*, 1995, **59**, 4623–4632.
61 P. M. Dove and C. A. Czank, *Geochim. Cosmochim. Acta*, 1995, **59**, 1907–1915.
62 C. V. Putnis, M. Kowacz and A. Putnis, *Appl. Geochem.*, 2008, **23**, 2778–2788.
63 M. Kowacz, C. V. Putnis and A. Putnis, *Cryst. Growth Des.*, 2009, **9**, 5266–5272.
64 B. S. Bageri, M. A. Mahmoud, R. A. Shawabkeh, S. H. Al-Mutairi and A. Abdulraheem, *Arabian J. Sci. Eng.*, 2017, **42**, 1667–1674.
65 M. Mahmoud, B. Ba Geri, K. Abdelgawad, M. S. Kamal, I. Hussein, S. Elkatatny and R. Shawabkeh, *Energy Fuels*, 2018, **32**, 9813–9821.
66 J. S. Herman and W. B. White, *Geochim. Cosmochim. Acta*, 1985, **49**, 2017–2026.
67 B. W. McConchie, H. H. Norris, V. G. Bundoc, S. Trivedi, A. Boesen, J. F. Urban and A. M. Keane-Myers, *Infect. Immun.*, 2006, **74**, 6632–6641.

